IEEE Access
Multidisciplinary | Rapid Review | Open Access Journal

Received December 3, 2018, accepted December 24, 2018, date of publication December 28, 2018,
date of current version January 23, 2019.

Digital Object Identifier 10.1109/ACCESS.2018.2890123

Kinematic Self-Calibration Method for Dual-Manipulators Based on Optical Axis Constraint

QIDAN ZHU[1], XINRU XIE[1], CHAO LI[1], GUIHUA XIA[1], AND QI LIU[2]
[1]College of Automation, Harbin Engineering University, Harbin 150001, China
[2]Institute of Chemical Materials, China Academy of Engineering Physics, Mianyang 621000, China

Corresponding author: Xinru Xie (xiexinru@hrbeu.edu.cn)

This work was supported in part by the National Natural Science Foundation of China, and in part by the China Academy of Engineering Physics under Grant U1530119.

ABSTRACT Kinematic parameters' calibration is a powerful method to improve the accuracy of the robot. This paper proposes an effective kinematic self-calibration method for dual-manipulators based on virtual constraints to estimate the actual kinematic parameters of the robots. This method only needs a camera mounted on one robot end-effector (EE) and a calibration target attached to another robot EE. First, a new calibration error model based on the straight line constraint is established to formulate the positions' misalignment error with the kinematic parameters' error. Then, the particle swarm optimization algorithm is developed to generate the optimal calibration poses of the robots under the constraints, which are used to ensure the poses feasible and the measurement errors acceptable. Finally, the kinematic parameter errors are identified with the Levenberg–Marquardt algorithm. The experiments of the kinematic parameters' calibration with the dual-manipulators system are designed. The experimental results showed that the high positional accuracy of both robots can be achieved.

INDEX TERMS Kinematic calibration, dual-manipulators, virtual constraint, PSO.

I. INTRODUCTION

Cooperating manipulators will be applied in more fields in the future. They are more efficient and allowed to perform complex tasks that exceed the capability of one robot. With more applications of the dual-manipulators on contact tasks, a higher request to the positioning accuracy of the robot is brought forward. During the cooperation process, even small poses error could lead to a large contact force between the robots and environment. For the dual-manipulators, except for the base frame calibration [1], [2] which is used to calibrate the relationship between the base frames of the two robots, improving the absolute positioning accuracy of each manipulator is extremely important.

Traditionally, the pose of the robot EE is calculated based on the kinematic model. The accuracy of the robot is largely depends on the kinematic parameters. However, the kinematic parameters are not accurate due to the manufacturing and assembly tolerance. The kinematic calibration methods for the dual-manipulators are usually same as those for the single manipulator by calibrating each manipulator respectively. The calibration methods can be divided into two categories: open-loop and close-loop.

In the open-loop methods, the actual poses of the robot relative to the base frame are measured by some devices. The high precision apparatuses were used at first, such as coordinate measuring machines [3], laser tracking interferometer systems [4], telescoping ball-bar [5] and other customized fixtures. These apparatuses are expensive, complicated to operate and time consuming. Moreover, the installation and operation of these measurement machines are restricted in some specific environments, such as harsh industry environment, space [6] and underwater [7].

Nowadays, the vision-based calibration methods have been developed because cameras are cost efficient and easy to use. The actual poses of the robot are estimated based on cameras which are attached to the robot EE or located in the workspace. Meng and Zhuang [8] proposed a vision-based self-calibration method, only image sequences of a calibration object and a ground-truth scale are needed. Du and Zhang [9] designed an efficient and automatic

approach to estimate the robot poses from the corners positions of a calibration board. Zhang *et al.* [10] realized online, automatic robot calibration by a stereo camera mounted on a fixed location in the environment and a planar marker attached to the robot EE. In these vision-based calibration methods, the accuracy of the camera parameters and/or hand-to-eye relative poses would have an effect on the robot calibration result. Additionally, the vision-based robot poses estimation methods usually suffer from the inaccurate camera depth information.

The closed-loop methods are promising methods which are based on the joint angles only and do not require the actual endpoint pose measurement. In these methods, the physical contact constraints, including single endpoint constraint [11], planar constraint [12], distance and sphere constraints [13], are imposed on the end of the robot. Then a closed kinematic chain is formed by the manipulator which is redundant with respect to its endpoint constraint [14]. However, these methods suffer from the inaccuracy positioning. Moreover, it is difficult to ensure that the robot EE fits the constraints exactly.

In order to improve the calibration methods based on the physical contact constraints, the concept of virtual constraint is put forward. Newman and Osborn [15] relied on the virtual straight line constraints which are provided by a laser beam. The calibration process was done by an optical detector mounted on the end of the robot centered on the laser line at sampled positions. An acceptable robot positioning accuracy was achieved at last. Gatla *et al.* [16] proposed a virtual closed kinematic chain method that a laser pointer tool attached to the robot EE was used to aim at a fixed object. Yin *et al.* [17] defined a Tool Center Point (TPC) in the structural model of a laser sensor, and aligned the TPC to a reference point to satisfy the endpoint constraint using a camera attached to the robot EE. Du *et al.* [18] constructed a virtual point and sphere constraints to calibrate the kinematic parameters using two fixed cameras and a position sensitive device (PSD). The calibration methods based on the virtual constraints are easy to implement, and the calibrate process could be executed automatically. Nevertheless, the employ of multi-tools in these techniques, such as laser device, camera and PSD, complicates the calibration process.

The dual-manipulators and multi-manipulators system should be calibrated on-site and the relative location between the two manipulators need to be maintained. Thus some methods that need specific calibration environment are not suit for the dual-manipulators. There are some researches about improving the accuracy of multi-robots recently. Except for the base-base calibration of dual-manipulators or dual-machines [2], [19]–[21], some researches are related to the kinematic parameters calibration and joint offset calibration. Bonitz and Hsia [22] introduced a method to determine the joint offset vector and the transformation matrix between the two robot base frames. A closed kinematic chain was formed by bolting calibration plates which are attached to the two manipulators EE together. Qiao *et al.* [23] proposed a calibration method to identify the exact kinematic parameters without using the nominal parameters. Zhao *et al.* [24] proposed a united kinematic calibration method for a dual-machine system in the drilling and riveting tasks. Both absolute and relative pose accuracies are improved. However, the current research on the dual-robots calibration is inadequate. It is extremely needed to come up with a high-precision calibration method for dual-manipulators which is inexpensive, easy-to-perform, and only requires few external devices which are easily available.

In this paper, a new kinematic parameters calibration method is developed based on the optical axis virtual constraints, combining the advantages of vision-based calibration method and virtual constraints based calibration method. In the case of the kinematic parameters of both manipulators are inaccurate, the calibration can be done using a camera and a common calibration target only. It is inexpensive and easily available because many robots have equipped with a camera to perform vision-based tasks. Compared with the real constraint calibration methods, this method is based on contactless constraint. In this way, the calibration errors engendered by structure deformation and contact error could be reduced. Before the robot kinematic calibration, the camera intrinsic parameters should be calibrated using the calibration algorithm [25]. The relative pose between the two manipulators and the rotation matrix between the active robot EE and camera are approximated roughly. These parameters are used in the proposed method to make the calibration process completed automatically.

The major contributions of the proposed method are shown as follows: (1) a new kinematic error model based on the straight line constraint is established to formulate the positions misalignment error with the kinematic parameters error. The actual poses of the robot are unnecessary in this error model. (2) The constraints are analyzed to limit the measurement errors related to camera resolution, and optimization strategy is designed to generate the optimal poses of the two robots. (3) A position alignment algorithm is designed based on the visual control method. Then the calibration process can be accomplished automatically and only need few operator supervision. (4) The experiments verify that the proposed method can improve the accuracy of both robots.

The remainder of the paper is organized as follows. Section II introduces the scheme of the proposed kinematic calibration method. Section III establishes a new kinematic error model. The optimal poses generation algorithm is presented in Section IV. Then Section V describes the poses alignment method and kinematic parameters identification algorithm. Section VI evaluates the accuracy improvement of the dual-manipulators by conducting experiments. Finally, discussion and conclusion are given in Section VII and Section VIII respectively.

II. SCHEME OF THE KINEMATIC CALIBRATION METHOD

Figure 1 shows a dual-manipulators system. Simple assistant devices, a camera and a calibration target, are used to calibrate

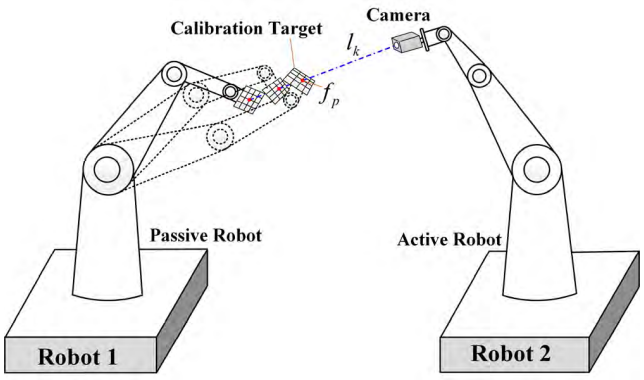

FIGURE 1. The basic configuration for the dual-manipulators during the calibration process.

the two manipulators. The first calibrated robot is called passive robot, and the other one is called active robot. The calibration target is attached to the end of the passive robot. The center corner of the calibration target is regarded as the visual feature point f_p. The camera is rigidly fixed on the end of the active robot. The direction of the optical axis l_k can be changed by controlling the pose of the active robot. After finishing calibrating the passive robot, the roles of the passive and active robots are exchanged to calibrate the other robot.

The process of kinematic parameter calibration for each manipulator can be divided into four steps and the scheme of the proposed kinematic parameter calibration method is shown in Fig. 2.

1) Kinematics calibration modeling. A new kinematic error model based on the straight line constraint is established to formulate the position alignment error with the kinematic parameters error. The alignment error is defined as the difference between the nominal value of the different positions of f_p.
2) Desired poses generation. In order to make the poses of the robots feasible and the measurement errors acceptable, four constraints related to the robots and camera are considered. An observation index is used to define the robot optimal calibration poses. Then the PSO algorithm is developed to generate the optimal poses.
3) Actual positions alignment. Because of the kinematic parameters error and other errors of the dual-robots system, the feature point are not strictly on the optical axis when the two robots both reached the desired poses. The image-based visual control method is applied to control the passive robot and make the feature point move to the optical axis automatically.
4) Kinematics parameters identification. The joint angles of the passive robot are recorded when the feature point is on the optical axis. Then the misaligned errors are calculated. Based on the established kinematic error model, the kinematic parameters errors are identified using the LM algorithm.

III. KINEMATIC ERROR MODEL

The kinematic error model is the basis of the kinematic parameters calibration process. A new kinematic error model based on straight line constraint is established in this section.

A. KINEMATIC MODEL

The kinematic model for calibration is used to formulate the relationship between the joint angles and the poses of the robot EE, which should meet three rules: model completeness, parameter minimality and model continuity [26]. Generally, the classic DH method is applied for robot kinematic modeling. In the DH method, however, the kinematic model is not continuous for the robots which possess parallel or near parallel joint axes.

Several kinematics models were proposed to solve this problem. Zhuang *et al.* [27] introduced a complete and parametrically continuous (CPC) model, added two parameters to make the model complete and continuous. The modified complete and parametrically continuous (MCPC) model was proposed to simplify the CPC model [28], while the completeness and continuity characteristics are retained. Considering the zero-error and joints angle error separately, a calibration error model based on the Product of Exponentials (POE) formula is proposed [29], which improved the calibration accuracy. Hayati [30] proposed an improved DH model, which is intuitive and simple. An additional parameter is added to describe the deviation between the parallel axes. In this paper, the improved DH modeling method is applied to establish the kinematics error model firstly, which is sufficient for the robots calibration. The complicated model transformation could be avoided because the robot kinematics are mostly established based on the DH model.

For the N-DOF serial manipulator, the continuous transformation matrix from the base coordinates to the end coordinates can be represented by

$$ {}^{0}\boldsymbol{T}_{N} = {}^{0}\boldsymbol{T}_{1} \cdot {}^{1}\boldsymbol{T}_{2} \cdot \ldots \cdot {}^{N-1}\boldsymbol{T}_{N} = \prod_{i=1}^{N} {}^{i-1}\boldsymbol{T}_{i}, \tag{1} $$

where ${}^{i-1}\boldsymbol{T}_{i}$ is the transformation matrix from the i-1^{th} link coordinates to the i^{th} link coordinates. If the adjacent joint axes are nearly parallel, the homogeneous transformation matrix ${}^{i-1}\boldsymbol{T}_{i}$ is expressed as

$$ {}^{i-1}\boldsymbol{T}_{i} = \begin{bmatrix} c_{\theta_i}c_{\beta_i} - s_{\theta_i}s_{\alpha_i}s_{\beta_i} & -s_{\theta_i}c_{\alpha_i} & c_{\theta_i}s_{\beta_i} + s_{\theta_i}s_{\alpha_i}c_{\beta_i} & \alpha_i c_{\theta_i} \\ s_{\theta_i}c_{\beta_i} - c_{\theta_i}s_{\alpha_i}s_{\beta_i} & c_{\theta_i}c_{\alpha_i} & s_{\theta_i}s_{\beta_i} - c_{\theta_i}s_{\alpha_i}c_{\beta_i} & \alpha_i s_{\theta_i} \\ -c_{\alpha_i}s_{\beta_i} & s_{\alpha_i} & c_{\alpha_i}c_{\beta_i} & d_i \\ 0 & 0 & 0 & 1 \end{bmatrix}. \tag{2} $$

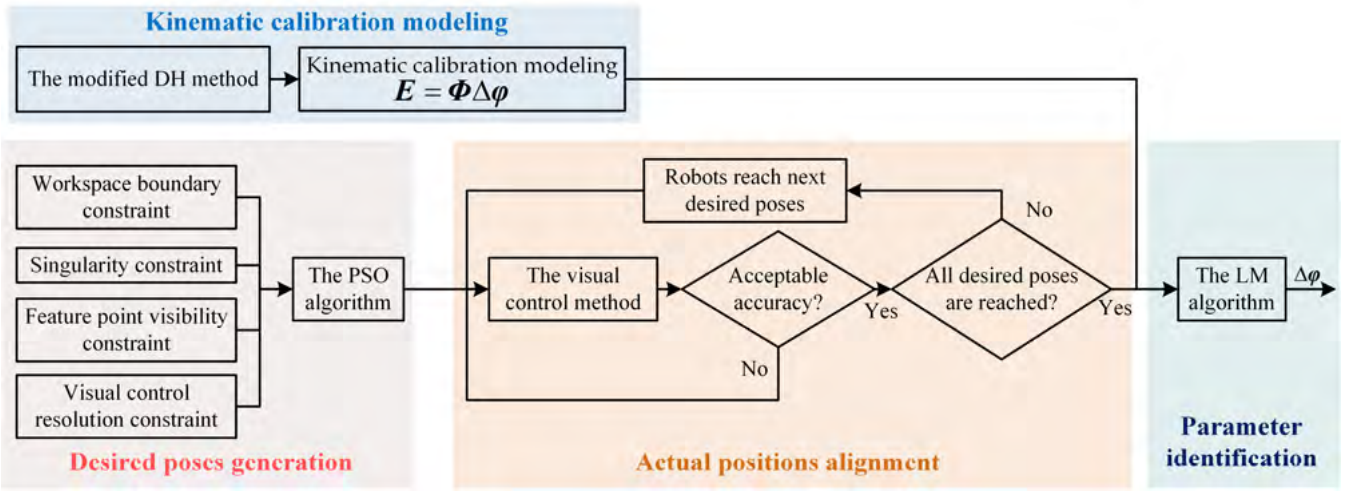

FIGURE 2. The scheme of the kinematic parameter calibration method.

If not, the homogeneous transformation matrix ${}^{i-1}\boldsymbol{T}_i$ is expressed as

$$ {}^{i-1}\boldsymbol{T}_i = \begin{bmatrix} c\theta_i & -s\theta_i c\alpha_i & s\theta_i s\alpha_i & a_i c\theta_i \\ s\theta_i & c\theta_i c\alpha_i & -c\theta_i s\alpha_i & a_i s\theta_i \\ 0 & s\alpha_i & c\alpha_i & d_i \\ 0 & 0 & 0 & 0 \end{bmatrix}, \quad (3) $$

where the joint angle θ_i, link offset d_i, link length a_i, link twist α_i and rotation angle β_i are the kinematic parameters of thei^{th} link.

B. ERROR MODEL BASED ON STRAIGHT LINE CONSTRAINTS

Define the actual and nominal transformation matrix from the base coordinates to the robot EE coordinates as ${}^0\boldsymbol{T}'_N$ and ${}^0\boldsymbol{T}_N$ respectively. The relationship between them can be represented by

$$ {}^0\boldsymbol{T}'_N = {}^0\boldsymbol{T}_N + \Delta{}^0\boldsymbol{T}_N = \prod_{i=1}^{N} ({}^{i-1}\boldsymbol{T}_i + \Delta{}^{i-1}\boldsymbol{T}_i), \quad (4) $$

where $\Delta{}^{i-1}\boldsymbol{T}_i$ is defined as the error transformation matrix from the *i-1*th link coordinates to the i^{th} link coordinates, and it can be expressed as

$$ \Delta{}^{i-1}\boldsymbol{T}_i = \frac{\partial {}^{i-1}\boldsymbol{T}_i}{\partial\theta_i}\Delta\theta_i + \frac{\partial {}^{i-1}\boldsymbol{T}_i}{\partial d_i}\Delta d_i + \frac{\partial {}^{i-1}\boldsymbol{T}_i}{\partial a_i}\Delta a_i + \frac{\partial {}^{i-1}\boldsymbol{T}_i}{\partial\alpha_i}\Delta\alpha_i + \frac{\partial {}^{i-1}\boldsymbol{T}_i}{\partial\beta_i}\Delta\beta_i, \quad (5) $$

where $\Delta\theta_i$, Δd_i, Δa_i, $\Delta\alpha_i$, $\Delta\beta_i$ are the errors between the actual and nominal kinematics parameters.

Expanding (4) and ignoring the high-order terms of the equation's right side, the error matrix $\Delta{}^0\boldsymbol{T}_N$ can be approximated as

$$ \Delta{}^0\boldsymbol{T}_N = \sum_{i=1}^{N} ({}^0\boldsymbol{T}_1 \ldots {}^{i-2}\boldsymbol{T}_{i-1}\Delta{}^{i-1}\boldsymbol{T}_i {}^i\boldsymbol{T}_{i+1} \ldots {}^{N-1}\boldsymbol{T}_N) $$

$$ = {}^0\boldsymbol{T}_N \delta{}^0\boldsymbol{T}_N, \quad (6) $$

$$ \delta{}^0\boldsymbol{T}_N = \begin{bmatrix} 0 & -\delta r_z & \delta r_y & \delta p_x \\ \delta r_z & 0 & -\delta r_x & \delta p_y \\ -\delta r_y & \delta r_x & 0 & \delta p_z \\ 0 & 0 & 0 & 0 \end{bmatrix}. \quad (7) $$

$\delta\boldsymbol{p}_e = [\delta p_x \delta p_y \delta p_y]^T$ and $\delta\boldsymbol{r}_e = [\delta r_x \delta r_y \delta r_z]^T$ are the translation and rotation errors respectively expressed in the robot EE frame.

Combining (5), (6) and (7) we can get

$$ \begin{bmatrix} \delta\boldsymbol{p}_e \\ \delta\boldsymbol{r}_e \end{bmatrix} = \begin{bmatrix} \boldsymbol{M}_\theta \\ \boldsymbol{R}_\theta \end{bmatrix} \Delta\boldsymbol{\theta} + \begin{bmatrix} \boldsymbol{M}_d \\ 0 \end{bmatrix} \Delta\boldsymbol{d} + \begin{bmatrix} \boldsymbol{M}_a \\ 0 \end{bmatrix} \Delta\boldsymbol{a} + \begin{bmatrix} \boldsymbol{M}_\alpha \\ \boldsymbol{R}_\alpha \end{bmatrix} \Delta\boldsymbol{\alpha} + \begin{bmatrix} \boldsymbol{M}_\beta \\ \boldsymbol{R}_\beta \end{bmatrix} \Delta\boldsymbol{\beta}, \quad (8) $$

where $\Delta\boldsymbol{\theta} = [\Delta\theta_1 \Delta\theta_2 \cdots \Delta\theta_N]^T$, $\Delta\boldsymbol{d} = [\Delta d_1 \Delta d_2 \cdots \Delta d_N]^T$, $\Delta\boldsymbol{a} = [\Delta a_1 \Delta a_2 \cdots \Delta a_N]^T$, $\Delta\boldsymbol{\alpha} = [\Delta\alpha_1 \Delta\alpha_2 \cdots \Delta\alpha_N]^T$, $\Delta\boldsymbol{\beta} = [\Delta\beta_1 \Delta\beta_2 \cdots \Delta\beta_N]^T$.

$\boldsymbol{M}_\theta, \boldsymbol{M}_d, \boldsymbol{M}_a, \boldsymbol{M}_\alpha, \boldsymbol{M}_\beta, \boldsymbol{R}_\theta, \boldsymbol{R}_\alpha, \boldsymbol{R}_\beta$ are $3 \times N$ matrices related to the nominal kinematic parameters and joint angles.

The linear Equation (8) can be rewritten in Jacobian notation

$$ \begin{bmatrix} \delta\boldsymbol{p}_e \\ \delta\boldsymbol{r}_e \end{bmatrix} = \begin{bmatrix} \boldsymbol{J}_P \\ \boldsymbol{J}_R \end{bmatrix} \Delta\boldsymbol{\varphi}, $$

$$ \Delta\boldsymbol{\varphi} = \begin{bmatrix} \Delta\boldsymbol{\theta} & \Delta\boldsymbol{d} & \Delta\boldsymbol{a} & \Delta\boldsymbol{\alpha} & \Delta\boldsymbol{\beta} \end{bmatrix}^T, $$

$$ \boldsymbol{J} = \begin{bmatrix} \boldsymbol{J}_P \\ \boldsymbol{J}_R \end{bmatrix} = \begin{bmatrix} \boldsymbol{M}_\theta & \boldsymbol{M}_d & \boldsymbol{M}_a & \boldsymbol{M}_\alpha & \boldsymbol{M}_\beta \\ \boldsymbol{R}_\theta & 0 & 0 & \boldsymbol{R}_\alpha & \boldsymbol{R}_\beta \end{bmatrix}. \quad (9) $$

The optical axis of a camera is a virtual straight line which is passing through the lens center and perpendicular to the mirror surface. Based on the straight line constraint, the kinematics error model is developed.

The calibration target attached to the passive robot EE is seemed as a passive link of the robot, and it is modeled in the robot kinematic model. f_p is supposed as the origin of the

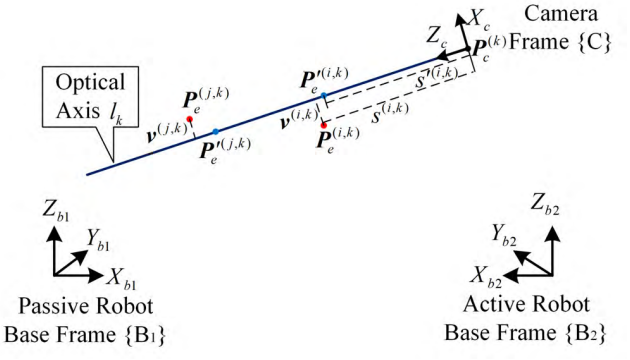

FIGURE 3. The positions of feature point in different frames.

passive robot EE coordinates. Let $\boldsymbol{P}_e^{\prime(i,k)}$ be the i^{th} actual position of f_p which is located on the k^{th} straight line constraint. The corresponding nominal position is $\boldsymbol{P}_e^{(i,k)}$, which can be calculated by (1). From (6) and (9) we can get

$$\Delta \boldsymbol{P}_e = {}^0\boldsymbol{R}_N \cdot \delta \boldsymbol{p}_e, \tag{10}$$

$$\delta \boldsymbol{P}_e = \boldsymbol{J}_P \cdot \Delta \boldsymbol{\varphi}. \tag{11}$$

From (10) and (11), the position error $\Delta \boldsymbol{P}_e^{(i,k)}$ can be written as

$$\Delta \boldsymbol{P}_e^{(i,k)} = \boldsymbol{P}_e^{\prime(i,k)} - \boldsymbol{P}_e^{(i,k)} = {}^0\boldsymbol{R}_N \boldsymbol{J}_P \Delta \boldsymbol{\varphi}, \tag{12}$$

where ${}^0\boldsymbol{R}_N$ is the nominal orientation transformation matrix from the robot base frame to the EE frame.

The actual and nominal positions of the feature point are shown in Fig. 3. $\boldsymbol{P}_c^{(k)}$ is the original point of the camera coordinates. $\boldsymbol{P}_e^{\prime(i,k)}$ and $\boldsymbol{P}_e^{\prime(j,k)}$ are the two actual positions of the feature point on the optical axis l_k. The corresponding nominal positions are $\boldsymbol{P}_e^{(i,k)}$ and $\boldsymbol{P}_e^{(j,k)}$, respectively. $\boldsymbol{P}_e^{(i,k)}$ and $\boldsymbol{P}_e^{\prime(i,k)}$ can be expressed as

$$\boldsymbol{P}_e^{(i,k)} = s^{(i,k)}\boldsymbol{\mu}_k + \boldsymbol{v}^{(i,k)} + \boldsymbol{P}_c^{(k)}, \tag{13}$$

$$\boldsymbol{P}_e^{\prime(i,k)} = s^{\prime(i,k)}\boldsymbol{\mu}_k + \boldsymbol{P}_c^{(k)}, \tag{14}$$

where $\boldsymbol{\mu}_k$ is the vector of the optical axis l_k. The transversal component of $\boldsymbol{P}_e^{(i,k)}$ is $\boldsymbol{v}^{(i,k)}$, which is perpendicular to l_k. The longitudinal component of $\boldsymbol{P}_e^{(i,k)}$ is $s^{(i,k)}\boldsymbol{\mu}_k$. Likewise, the longitudinal and transversal components of $\boldsymbol{P}_e^{\prime(i,k)}$ are $s^{\prime(i,k)}\boldsymbol{\mu}_k$ and zero matrix respectively.

Substituting (13) and (14) into (12), we have

$$(s^{(i,k)} - s^{\prime(i,k)})\boldsymbol{\mu}_k + \boldsymbol{v}^{(i,k)} = -{}^0\boldsymbol{R}_N \boldsymbol{J}_P \Delta \boldsymbol{\varphi}. \tag{15}$$

Define the cross product matrix $[\boldsymbol{\mu}_k\times]$ as $\forall \boldsymbol{N} \in \boldsymbol{R}^3$: $[\boldsymbol{\mu}_k\times]\boldsymbol{N} = \boldsymbol{\mu}_k \times \boldsymbol{N}$, and notice that $[\boldsymbol{\mu}_k\times]\boldsymbol{\mu}_k$=0. Multiplying $[\boldsymbol{\mu}_k\times]$ to both sides of (15) we have

$$[\boldsymbol{\mu}_k\times]\boldsymbol{v}^{(i,k)} = -[\boldsymbol{\mu}_k\times]{}^0\boldsymbol{R}_N \boldsymbol{J}_P \Delta \boldsymbol{\varphi}. \tag{16}$$

We can obtain two equations by writing (16) for two positions $\boldsymbol{P}_e^{(i,k)}$ and $\boldsymbol{P}_e^{(j,k)}$ on the same optical axis l_k. Subtracting these two equations side by side, we have

$$[\boldsymbol{\mu}_k\times]\left(\boldsymbol{v}^{(j,k)} - \boldsymbol{v}^{(i,k)}\right)$$

$$= [\boldsymbol{\mu}_k\times]\left[{}^0\boldsymbol{R}_N(\boldsymbol{\theta})\boldsymbol{J}_P(\boldsymbol{\theta})|_{\boldsymbol{\theta}=\theta_m^{(i,k)}} - {}^0\boldsymbol{R}_N(\boldsymbol{\theta})\boldsymbol{J}_P(\boldsymbol{\theta})|_{\boldsymbol{\theta}=\theta_m^{(j,k)}}\right] \cdot \Delta\varphi. \tag{17}$$

It is obvious that the deviation between the two different nominal positions of f_p is related to the kinematic parameters error. The deviation $\boldsymbol{E}^{(i,j,k)}$ is called misaligned error, which is defined in (18). And the deviation $\bar{\boldsymbol{J}}^{(i,j,k)}$ is called error Jacobian matrix , which is defined in (19).

$$\boldsymbol{E}^{(i,j,k)} = [\boldsymbol{\mu}_k\times]\Delta\boldsymbol{P}^{(i,j,k)} = [\boldsymbol{\mu}_k\times]\left(\boldsymbol{v}^{(j,k)} - \boldsymbol{v}^{(i,k)}\right) \tag{18}$$

$$\bar{\boldsymbol{J}}^{(i,j,k)} = [\boldsymbol{\mu}_k\times] \times \left[{}^0\boldsymbol{R}_N(\boldsymbol{\theta})\boldsymbol{J}_P(\boldsymbol{\theta})|_{\boldsymbol{\theta}=\theta_m^{(i,k)}} - {}^0\boldsymbol{R}_N(\boldsymbol{\theta})\boldsymbol{J}_P(\boldsymbol{\theta})|_{\boldsymbol{\theta}=\theta_m^{(j,k)}}\right]. \tag{19}$$

Then (17) can be expressed as

$$\boldsymbol{E}^{(i,j,k)} = \bar{\boldsymbol{J}}^{(i,j,k)}\Delta\boldsymbol{\varphi}. \tag{20}$$

Suppose that there are q straight line constraints and f_p is expected to align to each optical axis at p sampled positions. For all the positions of f_p we have the following equation

$$\boldsymbol{E} = \boldsymbol{\Phi}\Delta\boldsymbol{\varphi}, \tag{21}$$

$$\boldsymbol{E} = \left[\boldsymbol{E}^{(1,1,1)^T},\ldots,\boldsymbol{E}^{(p-1,p,1)^T},\ldots,\boldsymbol{E}^{(1,1,q)^T},\ldots,\boldsymbol{E}^{(p-1,p,q)^T}\right]^T, \tag{22}$$

$$\boldsymbol{\Phi} = \left[\bar{\boldsymbol{J}}^{(1,1,1)^T},\ldots,\bar{\boldsymbol{J}}^{(p-1,p,1)^T},\ldots,\bar{\boldsymbol{J}}^{(1,1,q)^T},\ldots,\bar{\boldsymbol{J}}^{(p-1,p,q)^T}\right]^T. \tag{23}$$

Based on the error model in (21), the kinematics parameters error $\Delta\boldsymbol{\varphi}$ can be identified. Note that the nominal position alignment error rather than the actual position of the feature point is used in the error model, the actual positions do not need to be measured. Moreover, the longitudinal component of the nominal position is not included in the error model. So the depth information of the camera has no influence on the parameters calibration result.

IV. GENERATION OF DESIRED POSES FOR TWO MANIPULATORS

In order to make the calibration poses feasible and improve the calibration accuracy, four constraints and an optimization index are considered in this section. Then the PSO algorithm is designed to get the optimal poses of the two manipulators.

A. CONSTRAINTS ANALYSIS

1) WORKSPACE BOUNDARY

The poses of the robots are infeasible when the robots out of their reachable workspace. The robots is within their workspace when all the joints are not beyond the joint limits. Define a joint limit index I_L as

$$I_L = 1/\min_{i<n}(D_{\theta_i}), \quad D_{\theta_i} = \min(\|\theta_i - \theta_{\min i}\|, \|\theta_{\max i} - \theta_i\|), \tag{24}$$

where θ_i is the angle of the i^{th} joint, $\theta_{\min i}$ and $\theta_{\max i}$ are the minimum and maximum joint angles respectively that the i^{th} joint can reach.

The larger the index I_L, the more infeasible the pose. So the workspace boundary constraint is defined as

$$C_1 : I_L(\theta^{(i,k)}) \leq I_{L\max}, \tag{25}$$

where $I_{L\max}$ is the maximum acceptable joint limit index.

2) SINGULARITY

In order to make the movement trajectory of the two manipulators continuous, the desired poses should avoid the singular configurations of the robot. The distance between the robot pose and the singular configuration is used to quantify the feasibility of the pose. Define an singularity index I_S as

$$I_s = 1/\lambda_{\min}(\boldsymbol{J}_\theta), \tag{26}$$

where $\lambda_{\min}(\boldsymbol{J}_\theta)$ is the smallest singular value of the Jacobian matrix $\boldsymbol{J}_\theta$, and it can be used to describe the trend of the singularity. The pose is close to the singular configurations when $\lambda_{\min}$ is close to 0.

So the larger the index I_S, the more infeasible the pose. The feasibility constraint is defined as

$$C_2 : I_S(\theta^{(i,k)}) \leq I_{S\max}, \tag{27}$$

where $I_{S\max}$ is the maximum acceptable singularity index.

3) FEATURE POINT VISIBILITY

The feature point f_p should always be visible during the calibration process. The visibility of f_p is related to the orientation and position of the calibration target π_f.

The visibility is the best when π_f is perpendicular to l_k. Define the orientation visibility index I_v as

$$I_v^{(i,k)} = \cos(\theta_v^{(i,k)}), \tag{28}$$

where θ_v is the visibility angle between l_k and the normal of π_f. The visibility is the best when $I_v = 1$, while the feature point is completely invisible when $I_v \leq 0$.

The orientation visibility constraint is defined as

$$C_3 : 1 \geq I_v^{(i,k)} \geq I_{v\max}, \tag{29}$$

where $I_{v\max}$ is a constant ranging from 0.7 to 1. It can be determined from experiments.

Additionally, the distance between π_f and the camera should be long enough to make π_f always in the camera's view during visual control process.

The distance visibility constraint is defined as

$$C_4 : D^{(i,k)} = \left\| \boldsymbol{P}_e^{(i,k)} - \boldsymbol{P}_c^{(k)} \right\| \geq D_{\min}, \tag{30}$$

where $D^{(i,k)}$ is the distance between the feature point and the original point of camera coordinates, $\boldsymbol{P}_e^{(i,k)}$ is the position of the feature point, $\boldsymbol{P}_c^{(k)}$ is the original of camera coordinates, and $D_{\min}$ is a constant that related to the size of π_f and the camera parameters.

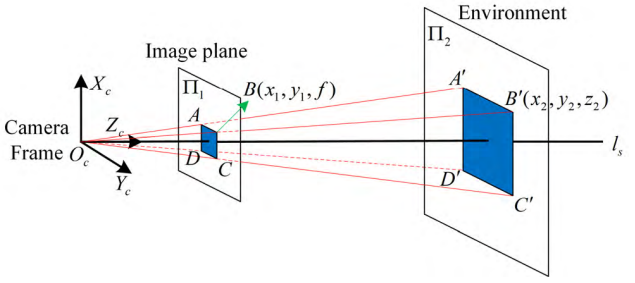

FIGURE 4. The schematic diagram of pinhole imaging.

4) VISUAL CONTROL RESOLUTION

Visual control method is used to control the feature point move to the optical axis automatically. The performance of the visual control relies on the resolution of the camera. The pixel difference $(\Delta u_f, \Delta v_f)$ between the image coordinate of f_p and the optical axis is

$$(\Delta u_f, \Delta v_f) = (u_f, v_f) - (u_0, v_0), \tag{31}$$

where (u_f, v_f) is the pixel coordinate of f_p, (u_0, v_0) is the pixel coordinate of the center point of optical axis. In the calibration process, it is regarded that f_p has aligned to the optical axis when $(\Delta u_f, \Delta v_f)$ is within a certain range $(\Delta u_{\max}, \Delta v_{\max})$, which is the visual control resolution error in the digital image. The corresponding resolution error in the real world can be calculated based on the pinhole imaging principle of camera.

As shown in Fig. 4, Σ_c is the camera coordinates, and the direction of z-axis is parallel to the optical axis. Suppose that the projection of the pixel $(\Delta u_{\max}, \Delta v_{\max})$ on the image plane Π_1 is $ABCD$, and the corresponding area in the environment Π_2 is $A'\,B'\,C'\,D'$. The position of B in the coordinates Σ_c is (x_1, y_1, z_1), where $z_1 = f$ is the focal length of camera. The corresponding position of B'in the environment is (x_2, y_2, z_2). The relationship between $B(x_1, y_1, z_1)$ and $B'(x_2, y_2, z_2)$ can be formulated as

$$\frac{x_1}{f} = \frac{x_2}{z_2}, \quad \frac{y_1}{f} = \frac{y_2}{z_2}. \tag{32}$$

In the visual control process, $B(x_1, y_1, z_1)$ is known, which can be calculated based on the camera parameters and pixel coordinate $(\Delta u_{\max}, \Delta v_{\max})$. Then (x_2, y_2) can be obtained based on (32). For the feature point which is on the optical axis, z_2 is equal to the distance $D^{(i,k)}$ which is shown in (30). The visual control resolution constraint can be expressed as

$$C_5 : D^{(i,k)} \leq D_{\max}, D_{\max} = z_{\max} = \min\left(\frac{x_{2\max} f}{x_1}, \frac{y_{2\max} f}{y_1}\right), \tag{33}$$

where $x_{2\max}$ and $y_{2\max}$ are the maximum acceptable visual control errors when f_p is on the optical axis. They should be less than the repeatability error of the robot.

B. OPTIMIZATION OF THE POSE

The calibration quality of the kinematic parameters depends on the choice of calibration poses. From the kinematic error model, we can see that the larger the determinant of the identification Jacobian matrix $\boldsymbol{J}$, the smaller the calibration error. An observability index can be defined to evaluate the optimality of the calibration configurations. Joubair and Bonev [31] proved that the observability index O_1 is most likely the best criterion to yield the best calibration results, which can be expressed as

$$O_1 = \frac{(\sigma_1\sigma_2\ldots\sigma_m)^{1/m}}{\sqrt{m}}, \tag{34}$$

where $\sigma_i(i = 1, 2\ldots, m)$ is the singular value of $\boldsymbol{J}, \sigma_1 \geq \sigma_2 \geq \cdots \geq \sigma_m \geq 0$. Larger value of O_1 yields better calibration result.

C. PSO ALGORITHM DESIGN

The constraints and the observability index considered above make the selection process of the optimal poses complex because it is highly nonlinear. It can be formulated as a constrained optimization problem that the desired poses $\boldsymbol{P}_\theta$ should satisfy all constraints $C_1(i = 1, 2, 3, 4)$ and make the observation index O_1 largest

$$\boldsymbol{P}_\theta = \{\theta^{(i,k)}, i \leq p, k \leq q\} = \underset{c_j(j=1,2,3,4)}{\arg\min} \left(\frac{1}{O_1}\right). \tag{35}$$

In order to solve this problem, the PSO algorithm is designed in this work. In the PSO algorithm, N particles are included in a particle swarm and each particle has q sub-particles corresponding to q directions of the optical axis. The process of the robots optimal configurations generation based on the PSO algorithm can be divided into four steps, and the flow chart is shown in Fig. 5.

1) The particle $\boldsymbol{X}_j$ is initialized with a random vector and it is defined as

$$\boldsymbol{X}_j = [\boldsymbol{X}_{S_j}^{(1)^T}, \ldots, \boldsymbol{X}_{S_j}^{(q)^T}], \tag{36}$$

$$\boldsymbol{X}_{S_j}^{(k)} = [\boldsymbol{\mu}_j^{(k)^T}, \boldsymbol{P}_{cj}^{(k)^T}, \boldsymbol{Q}_j^{(1,k)^T}, \ldots, \boldsymbol{Q}_j^{(p,k)^T}]. \tag{37}$$

The sub-particle $\boldsymbol{X}_{S_j}^{(k)}(k = 1, 2, \ldots, q)$ belongs to the particle $\boldsymbol{X}_j$,which contains the information about the p poses aligned to l_k of the passive robot. $\boldsymbol{\mu}_j^{(k)}(k = 1, 2, \ldots, q, j = 1, 2, \ldots, N)$ is the vector of the optical axis l_k, $\boldsymbol{P}_{cj}^{(k)}$ is the original point of the camera coordinates, and $\boldsymbol{Q}_j^{(i,k)}(i = 1, 2, \ldots, p)$ is the orientation of the passive robot EE. They are all described in the passive robot base frame and used to express the poses of both robots. The position of the feature point f_p is calculated by

$$\boldsymbol{P}_{ej}^{(i,k)} = \boldsymbol{P}_{cj}^{(k)} + (D + iD_{step})\boldsymbol{\mu}_j^{(k)}, \tag{38}$$

where D_{step} is the desired distance between the two adjacent positions of f_p. D is the distance between the original point of camera and the last position of f_p aligned to l_k. So the constraints C_3 and C_4 can be always achieved by setting appropriate D_{step} and D.

2) During each searching process, the fitness function f_{ob}, the best position of the particle X_{bi} and the best position $\boldsymbol{X}_{best}$ of all particles are updated to evaluate the particles. where f_{ob} is expressed as

$$f_{ob} = \frac{1}{O_1} = \frac{\sqrt{m}}{(\sigma_1\sigma_2\ldots\sigma_m)^{1/m}}. \tag{39}$$

Then the particles move to $\boldsymbol{X}_{bi}$ and $\boldsymbol{X}_{best}$ with respect to the following updating equations

$$\boldsymbol{V}_j(t+1) = w\boldsymbol{V}_j(t) + L_1\eta_1(\boldsymbol{X}_{bj}(t) - \boldsymbol{X}_j(t)) + L_2\eta_2(\boldsymbol{X}_{best}(t) - \boldsymbol{X}_j(t)), \tag{40}$$

$$\boldsymbol{X}_j(t+1) = \boldsymbol{X}_j(t) + \boldsymbol{V}_j(t+1), \tag{41}$$

where $\boldsymbol{V}_j(t)$ and $\boldsymbol{X}_j(t)$ are the velocity and position of the i^{th} particle at the t^{th} iteration. ω is the inertial factor. L_1 and L_2 are the positive constants of learning factors. η_1 and η_2 are the random constants between 0 and 1.

3) Check if the position $\boldsymbol{X}_j(t)$ satisfies the constraints C_1 and C_2 after each iteration. If not, the particles which are violating C_1 and C_2 should be updated again.

4) The optimal desired poses of both robots can be obtained.

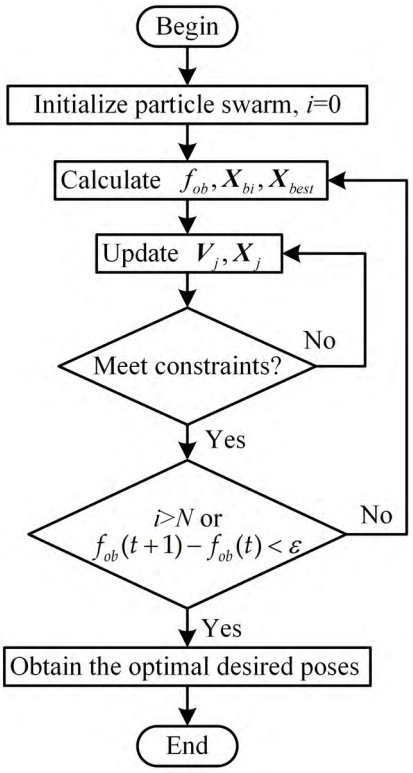

FIGURE 5. The flow chart of robots optimal configurations generation based on the PSO algorithm.

V. KINEMATIC PARAMETERS CALIBRATION

Because of the nominal kinematic parameters error and other errors of the robots system, the feature point f_p is not on the optical axis l_k when both robots reach the desired poses generated above. The image based visual control method is an ideal method to control the passive robot to make f_p move to l_k automatically. After f_p has coincided with the optical axis from all the desired poses, the misaligned error E in the kinematics error model is calculated. Then the kinematics parameters error vector $\Delta\boldsymbol{\varphi}$ is identified using LM algorithm.

A. POSES ALIGNMENT BASED ON VISUAL CONTROL METHOD

As shown in Fig. 6, the feature point should move to the optical axis from the generated positions.

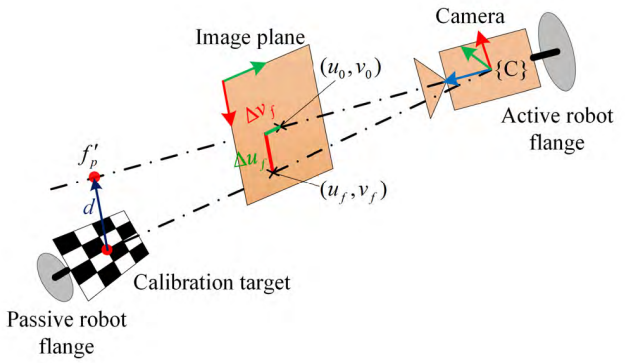

FIGURE 6. The schematic diagram of the feature point move to the optical axis.

Based on the perspective projection principle of camera, the ideal coincidence criteria is that the pixel coordinate (u_f, v_f) of the feature point coincides with the principle point (u_0, v_0) of image and the pixel difference $(\Delta u_f, \Delta v_f)$ is (0,0). The actual distance between the position of f_p and μ_k is defined as d. The goal of the visual control method is to make the distance d reduce to 0 gradually.

The scheme of the image based visual control method is illustrated in Fig. 7, which consists of an image feature control outer loop and a robot control inner loop. In the outer loop, the actual pixel coordinate (u_f, v_f) of the feature point is obtained based on the corner detection algorithm. Then the deviation between (u_f, v_f) and (u_0, v_0) is calculated and converted into the position deviation of the passive robot based on the pose adjustment strategy. In the inner closed loop, the desired pose of the passive robot is translated into the joint angles using the nominal inverse kinematics. Then the passive robot is controlled to reach the desired poses using the joint position controller.

In the pose adjustment strategy, the position deviation $\Delta\boldsymbol{P}_f^{bp}$ of the passive robot is calculated by

$$\Delta\boldsymbol{P}_f^{bp} = \boldsymbol{R}_c^{bp}\Delta\boldsymbol{P}_f^{c} = \boldsymbol{R}_c^{bp}\begin{bmatrix}(u_f - u_0)z_f/k_x\\(v_f - v_0)z_f/k_y\\0\end{bmatrix}. \tag{42}$$

The rotation matrix $\boldsymbol{R}_c^{bp}$ can be calculated by

$$\boldsymbol{R}_c^{bp} = \boldsymbol{R}_c^{h}\boldsymbol{R}_h^{ba}\boldsymbol{R}_{ba}^{bp}, \tag{43}$$

where $\boldsymbol{R}_h^{ba}$ is the rotation matrix from the active robot EE to the active robot base, which can be obtained based on the forward kinematic model. $\boldsymbol{R}_c^{h}$ relates the camera to active robot EE, and $\boldsymbol{R}_{ba}^{bp}$ relates the active robot base to passive robot base. $\boldsymbol{R}_c^{h}$ and $\boldsymbol{R}_{ba}^{bp}$ are approximated roughly using the measurement device in advance.

The intrinsic parameter matrix $\boldsymbol{M}_{in}$ of the camera is also needed, which is calibrated by the camera calibration method [25] before the robot calibration process.

$$\boldsymbol{M}_{in} = \begin{bmatrix}k_x & 0 & u_0\\0 & k_y & v_0\\0 & 0 & 1\end{bmatrix}. \tag{44}$$

Because the visual control system is closed-loop, the parameters k_x, k_y, z_f and $\boldsymbol{R}_c^{bp}$ in (42) are not required to be accurate completely. The pose of the passive robot can be adjusted to make the feature point align to the optical axis gradually and automatically.

B. PARAMETERS IDENTIFICATION

The joint angles of the passive robot are recorded when f_p is on the optical axis at all of the sampled position. The nominal positions $\boldsymbol{P}_e^{(i,k)}(x_i, y_i, z_i)$ of the passive robot can be further calculated using the nominal kinematic parameters and the saved joint angles. The optical axis vector $\boldsymbol{\mu}_k(m, n, 1)$ is estimated by $\boldsymbol{P}_e^{(i,k)}$ based on the least square method

$$\begin{bmatrix}m & x_0\\n & y_0\end{bmatrix} = \begin{bmatrix}\sum_{i=0}^{p} x_i z_i & \sum_{i=0}^{p} x_i\\ \sum_{i=0}^{p} y_i z_i & \sum_{i=0}^{p} y_i\end{bmatrix}\begin{bmatrix}\sum_{i=0}^{p} z_i^2 & \sum_{i=0}^{p} z_i\\ \sum_{i=0}^{p} z_i & p\end{bmatrix}^{-1}. \tag{45}$$

After estimating the optical axis vector $\boldsymbol{\mu}_k$, the misaligned error $\boldsymbol{E}^{(i,j,k)}$ can be calculated based on (18). Notice that $[\boldsymbol{\mu}_k\times]\boldsymbol{\mu}_k = 0$, from (13) and (18) we can have

$$\begin{aligned}&\boldsymbol{E}^{(i,j,k)}\\&= [\boldsymbol{\mu}_k\times]\left(\boldsymbol{v}^{(j,k)} - \boldsymbol{v}^{(i,k)}\right)\\&= [\boldsymbol{\mu}_k\times]\left((s^{(j,k)}\boldsymbol{\mu}_k + \boldsymbol{v}^{(j,k)} + \boldsymbol{P}_c^{(k)}) - (s^{(i,k)}\boldsymbol{\mu}_k + \boldsymbol{v}^{(i,k)} + \boldsymbol{P}_c^{(k)})\right)\\&= [\boldsymbol{\mu}_k\times]\left(\boldsymbol{P}_e^{(j,k)} - \boldsymbol{P}_e^{(i,k)}\right)\end{aligned} \tag{46}$$

As the optical axis vector $\boldsymbol{\mu}_k$ and the nominal positions $\boldsymbol{P}_e^{(i,k)}$ and $\boldsymbol{P}_e^{(j,k)}$ are all obtained, $\boldsymbol{E}^{(i,j,k)}$ can be calculated using (46). Then the misaligned error matrix $\boldsymbol{E}$ could be obtained based on (22).

In order to make the approximated vector $\hat{\boldsymbol{\mu}}_k$ more accurate, $\hat{\boldsymbol{\mu}}_k$ and $\Delta\boldsymbol{\varphi}$ are estimated in a recursive way. That is to say, $\hat{\boldsymbol{\mu}}_k$ is updated based on the updated positions of the passive robot iteratively, until the calibration error is small enough. The calibration error ε can be calculated as follows

$$\varepsilon = \left((\boldsymbol{E} - \boldsymbol{\Phi}\Delta\hat{\boldsymbol{\varphi}})^T(\boldsymbol{E} - \boldsymbol{\Phi}\Delta\hat{\boldsymbol{\varphi}})\right)^{\frac{1}{2}}. \tag{47}$$

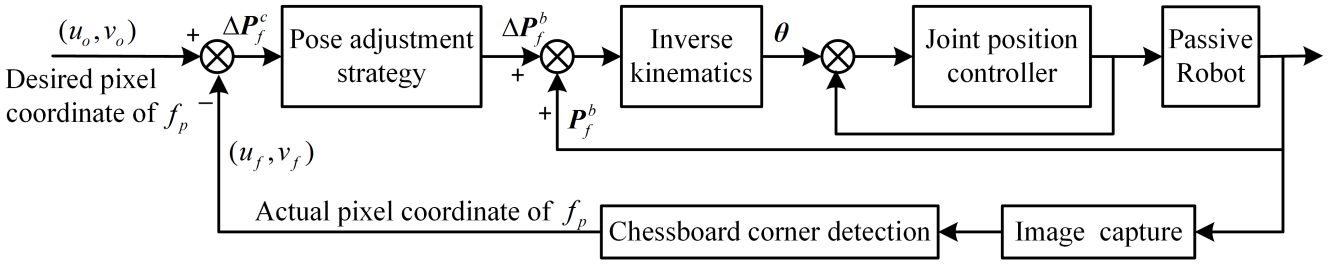

FIGURE 7. Scheme of the image based visual control method.

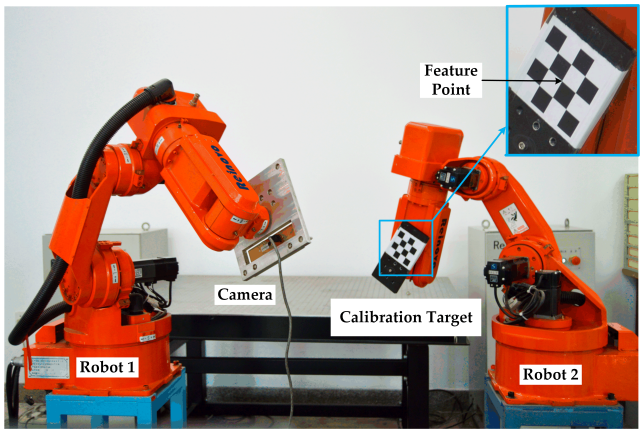

FIGURE 8. The kinematic calibration system with two Reinovo manipulators.

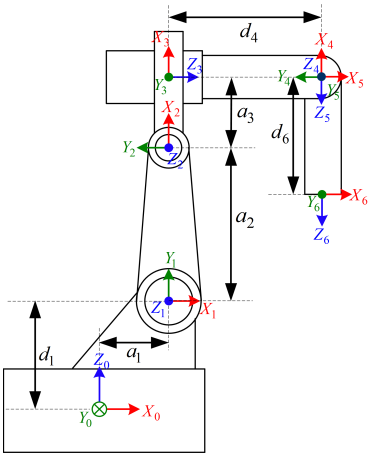

FIGURE 9. The local frames of the Reinovo robot in the initial configuration.

Then the LM algorithm is used to identify $\Delta\boldsymbol{\varphi}$. At the t^{th} iteration, the estimated $\Delta\hat{\boldsymbol{\varphi}}(t)$ is updated as

$$\Delta\hat{\boldsymbol{\varphi}}(t) = (\boldsymbol{\Phi}(t)^T\boldsymbol{\Phi}(t) + \lambda_{LM}(t)\boldsymbol{I})^{-1}\boldsymbol{\Phi}(t)^T\boldsymbol{E}, \tag{48}$$

where $\boldsymbol{I}$ is an identity matrix, $\lambda_{LM}(t)$ is the LM parameters, $\lambda_{LM}(0) \in [0.001, 0.1]$. The updated $\lambda_{LM}(t+1)$ at $i+1^{\text{th}}$ iteration is shown in (49), the scalar h ranges from 2 to 10.

$$\lambda_{LM}(t+1) = \begin{cases} \lambda_{LM}(t)/h, \varepsilon(t) < \varepsilon(t-1) \\ \lambda_{LM}(t)/h, \varepsilon(t) \geq \varepsilon(t-1). \end{cases} \tag{49}$$

VI. EXPERIMENTS

A. EXPERIMENT ENVIRONMENT

In order to verify the proposed robots calibration method, experiments are performed with a dual-manipulators calibration system. As shown in Fig. 8, the system consists of two Reinovo 6-DOF industrial manipulators, a Bumblebee CCD camera and a calibration target. The Reinovo robot has a repeatability accuracy of 0.1 mm. The camera with 1024H $\times$ 768V resolution and 3.8 mm focal length is fixed on the active robot flange rigidly. A 4 $\times$ 4 chessboard as the calibration target is attached to the passive robot flange and its fifth corner is served as the feature point f_p. In the current configuration, robot 1 is the active robot and robot 2 is the passive robot. The local frame of the Reinovo robot in the initial configuration is illustrated in Fig. 9.

The calibration target is considered as the link 7 of the passive robot, which is also modeled in the robot kinematic model. The nominal kinematic parameters of both robots are shown in Table 1 and Table 2 respectively. The calibrated camera intrinsic parameter matrix $\boldsymbol{M}_{in}$ is:

$$\boldsymbol{M}_{in} = \begin{bmatrix} k_x & 0 & u_0 \\ 0 & k_y & v_0 \\ 0 & 0 & 1 \end{bmatrix} = \begin{bmatrix} 834.31 & 0 & 513.56 \\ 0 & 833.38 & 403.95 \\ 0 & 0 & 1 \end{bmatrix}$$

TABLE 1. The nominal kinematic parameters of robot 1.

Link i	$\alpha_i(^\circ)$	$a_i(mm)$	$d_i(mm)$	$\theta_i(^\circ)$	$\beta_i(^\circ)$
1	90	100	136.5	0	/
2	0	290	/	90	0
3	90	121	0	0	/
4	-90	0	310	0	/
5	90	0	0	-90	/
6	0	60	121.5	0	/
7	0	0	0	-90	/

B. GENERATION OF THE DESIRED POSES

Before generating the desired poses of the robots, the base-base relative pose ${}^{b_1}\boldsymbol{T}_{b_2}$ and hand-eye relative pose ${}^{c}\boldsymbol{T}_{h}$ should be approximated roughly. The used Bumblebee camera is a binocular camera, and we just use one eye in the

TABLE 2. The nominal kinematic parameters of robot 2.

Link i	$\alpha_i(^\circ)$	$a_i(mm)$	$d_i(mm)$	$\theta_i(^\circ)$	$\beta_i(^\circ)$
1	90	100	136.5	0	/
2	0	290	/	90	0
3	90	121	0	0	/
4	-90	0	310	0	/
5	90	0	0	-90	/
6	0	60	131	0	/
7	0	0	0	-90	/

experiment. In this experiment, the right eye of the camera is used, the relative poses ${}^{b_1}\boldsymbol{T}_{b_2}$ and ${}^{c}\boldsymbol{T}_{h}$ are approximated by the following homogeneous matrix respectively

$$ {}^{b_1}\boldsymbol{T}_{b_2} = \begin{bmatrix} -1 & 0 & 0 & 1.2 \\ 0 & -1 & 0 & 0 \\ 0 & 0 & 1 & 0 \\ 0 & 0 & 0 & 1 \end{bmatrix}, $$

$$ {}^{c}\boldsymbol{T}_{h} = \begin{bmatrix} 1 & 0 & 0 & -0.6 \\ 0 & 1 & 0 & 0.6 \\ 0 & 0 & 1 & 0.26 \\ 0 & 0 & 0 & 1 \end{bmatrix}. $$

In the process of the desired poses generation, the constraints are set as follows

$$ \begin{aligned} C_1 &: I_S(\theta^{(i,k)}) \le I_{S\max}, I_{S\max} = 10, \\ C_2 &: I_L(\theta^{(i,k)}) \le I_{L\max}, I_{L\max} = 18/\pi, \\ C_3 &: 1 \ge I_v^{(i,k)} \ge I_{v\max}, I_{v\max} = \sqrt{3}/2, \\ C_4 &: D^{(i,k)} \ge D_{\min}, D_{\min} = 0.3m, \\ C_5 &: D^{(i,k)} \le D_{\max}, D_{\max} = 0.6m, \end{aligned} \tag{50} $$

where the minimal distance between each joint angle and its limit in C_1 is $\min_{i<n}(D_{\theta_i}) = 10^\circ$, the acceptable smallest singular value in C_2 is set as $\lambda_{\min} = 0.1$ and the visibility angle in C_3 is set as $-30^\circ < \theta_v < 30^\circ$.

There are totally 35 parameters expected to be identified for each robot. According to (19), each misaligned error $\boldsymbol{E}^{(i,j,k)}$ with three components is provided by every two robot positions. So at least 12 misaligned errors, which are calculated from six different passive robot positions, are needed to obtain the unique solution of the parameters. In order to improve the estimated accuracy of the optical axis vector, more configurations of the robots are required. Five optical axis in different directions and 10 poses aligned to each optical axis are generated for each robot.

Using the PSO algorithm, the optimal desired poses under the given constraints are generated. The swarm size is 10. The algorithm run 5 times and 100 iterations each time to search the best fitness value. In order to make the generated poses satisfy the constraints C_4 and C_5, the maximum distance between the calibration target and the camera is set as $D_{\max} = 0.5m$, the distance between the neighboring poses of the passive robot aligned to one optical axis is set as $D_{step} = 0.02m$. In the five running, the best fitness value achieved at each iteration is shown in Fig. 10.

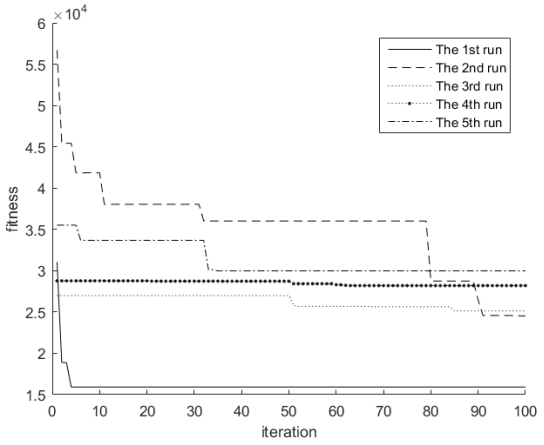

FIGURE 10. The fitness during each run of the PSO algorithm.

It can be seen that the best fitness $f_{ob\ best} = 1.6 \times 10^4$ during the PSO process is achieved in the first running. The generated optimal poses of both manipulators at the best fitness are depicted in Fig. 11. Note that the directions of the optical axis are different, and the desired positions of the passive robot has covered most of the robot workspace. So the particular problem of the desired positions is avoided.

C. CALIBRATION PROCESS AND RESULTS

With the generated poses, there are 50 different measurements for each robot. These data are divided into two sets: 30 measurements are used to be the calibration set, and the remaining 20 measurements are used to be the validation set.

The steps of the measurement process for each robot is:

1) Move the active robot to the desired position.
2) Move the passive robot to the corresponding desired position. Control the passive robot by the visual control method to make the feature point move to the optical axis of the camera automatically.

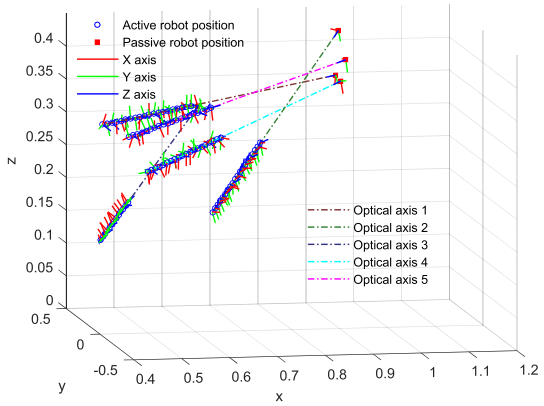

FIGURE 11. The optimal desired poses generated at the best fitness for the dual-robots.

3) Save the joint angles of the passive robot.
4) Repeat step 2) - 3) until the feature point has aligned to the current optical axis at 10 positions.
5) Repeat step 1) - 4) until the 50 measurements had done.

During the visual control process, a calibration interface program is designed to detect the feature point and control the feature point move to the optical axis automatically. The approximated base-base relative pose ${}^{b_1}\boldsymbol{T}_{b_2}$ of the robots and the hand-eye relative pose ${}^{c}\boldsymbol{T}_{h}$ are used to adjust the pose of the passive robot. The image in the view of camera before and after the visual control is shown in Fig. 12(a) and Fig. 12(b), respectively. The center of the red circle is the principle point, and the center of the green one is the actual position of f_p. The pixel differences $(\Delta u_f, \Delta v_f)$ between f_p and the optical axis reduced from $(-5.87, 13.04)$ to $(-0.01, 0.07)$. Generally, it costs 1 minutes during f_p moving from each generated position to the optical axis. Experiments show that the feature point can align to the optical axis automatically.

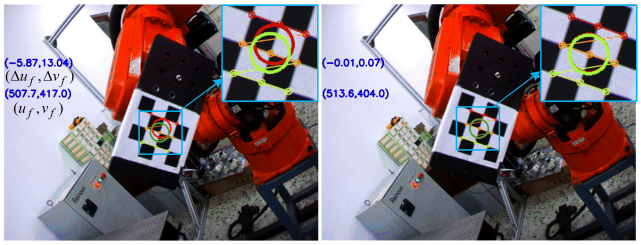

FIGURE 12. The image plane in the view of camera: (a) before the visual control; (b) after the visual control.

It is considered that f_p has aligned to the optical axis when the pixel differences $(\Delta u_f, \Delta v_f)$ between them is less than (0.1, 0.1). According to the parameters of the camera, the maximum visual control error e_d is calculated by Equation (51), it is acceptable because it is less than the repeatability accuracy of the robot.

$$e_d = \left(x_{2\max}^2 + y_{2\max}^2\right)^{\frac{1}{2}} = 0.087\text{mm}. \tag{51}$$

The snapshot of the system while f_p is on an optical axis at different positions is shown in Fig. 13. The red dotted line is the virtual constraint which are constructed by the optical axis of the camera. The colored solid circle points are the positions of f_p when it is on the optical axis.

Then the kinematic parameters errors are identified using the LM method. The calibration process is continued after exchanging the passive and active roles of the two robots. The estimated kinematic parameters errors of both robots are shown in Table 3 and Table 4 respectively.

With 10 positions of the feature point aligned to each optical axis, there are 45 misaligned errors corresponding to each optical axis. For the 30 calibration measurements, there are totally 135 misaligned errors for each robot. After the kinematic parameters are calibrated, the misaligned errors are recalculated by the calibrated kinematic parameters. The comparative result before and after calibration of the misaligned errors of the two robots are shown in Fig. 14. For the

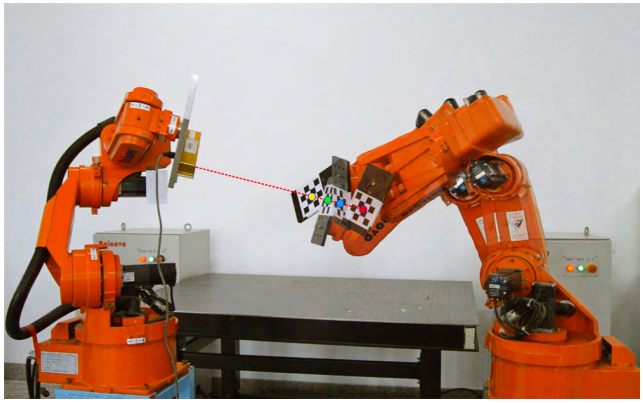

FIGURE 13. The snapshot of the system while the feature point is on an optical axis at different positions.

TABLE 3. The kinematic parameters errors of robot 1.

Link i	$\alpha_i(^\circ)$	$a_i(mm)$	$d_i(mm)$	$\theta_i(^\circ)$	$\beta_i(^\circ)$
1	-0.03	5.9	0	-0.15	/
2	0.26	-2.2	/	-0.11	0.05
3	-0.34	0.4	4.7	0.37	/
4	-0.59	-0.2	2.3	-0.49	/
5	-0.37	-2.1	-1.2	-0.33	/
6	0	0	2.2	-0.14	/
7	0	0.1	2.2	0	/

TABLE 4. The kinematic parameters errors of robot 2.

Link i	$\alpha_i(^\circ)$	$a_i(mm)$	$d_i(mm)$	$\theta_i(^\circ)$	$\beta_i(^\circ)$
1	0.35	5.7	0	-1.37	/
2	-0.53	-1.0	/	-0.10	0.52
3	0.58	3.5	-3.6	-0.29	/
4	-1.10	-0.1	3.6	-1.51	/
5	1.21	1.0	0.7	-1.35	/
6	0	0.4	2.8	-0.48	/
7	0	0.5	2.8	0	/

robot 1, the average misaligned error reduced from 2.22 mm and 0.33 mm, which decreased by 85.14%. For the robot 2, the average misaligned error after calibration reduced from 2.28 mm to 0.25 mm, which was a 89.04% decrease.

The misaligned errors of both robots after calibration are much less than those before calibration. In order to further illustrate the efficiency of the proposed method, we compared the calibration results with the robot calibration method in [9] and [17]. The best result in [9] is reduced from 7.33 mm to 1.53 mm. According to the calibration result in [17], the misaligned error before calibration is less than 0.8 mm and the misaligned error after calibration is 0.105 mm. The comparison of calibration result is shown in Table 5.

It is demonstrated that the result in this paper is better than those in [9] and almost as well as the result in [17]. Compared with [17], our method does not need the laser stripe generator, which makes the calibration more cheap and

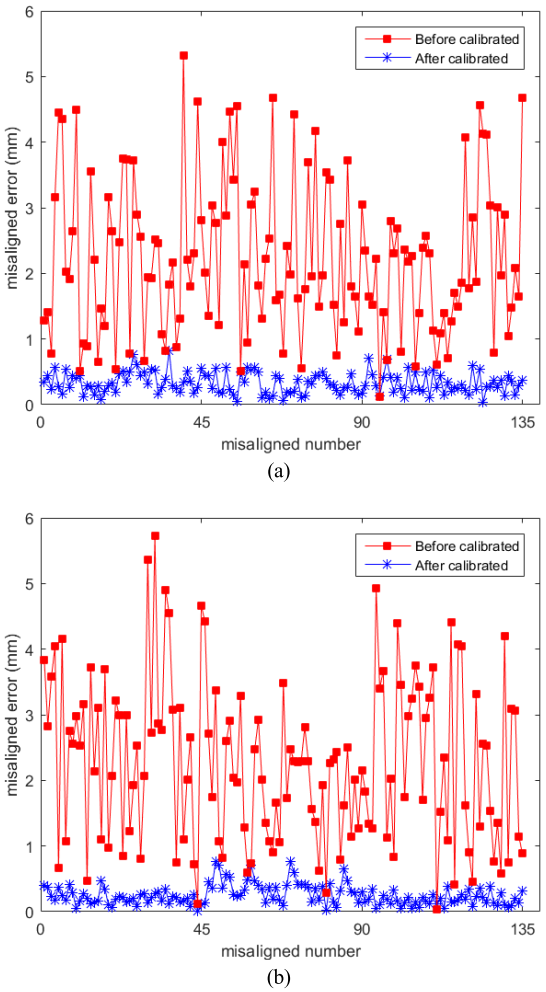

FIGURE 14. Misaligned errors with three optical axes before and after calibration of: (a) robot 1; (b) robot 2.

TABLE 5. The comparison of calibration results with method [9] and [17].

Average error	Method [9]	Method [17]	Robot 1 in Our Method	Robot 2 in Our Method
Before calibrated (mm)	7.33	0.8	2.22	2.28
After calibrated (mm)	1.53	0.105	0.33	0.25
Decrease(%)	79.13	86.87	85.14	89.04

easy to perform. Another advantage of the proposed method is that the robot can be calibrated automatically.

Then the remainder 20 measurements which are different from the experiment data are used to verify the calibrated result. The misaligned errors before and after calibration are calculated based on the nominal and calibrated parameters respectively. The comparison results of the two robots are shown in Fig. 15. As we can see, the mean values of the misaligned errors of robot 1 reduced from 1.95 mm to 0.58 mm and those of robot 2 reduced from 2.48 mm to 0.67 mm. As a consequence, the calibration method has improved the accuracy for both robots.

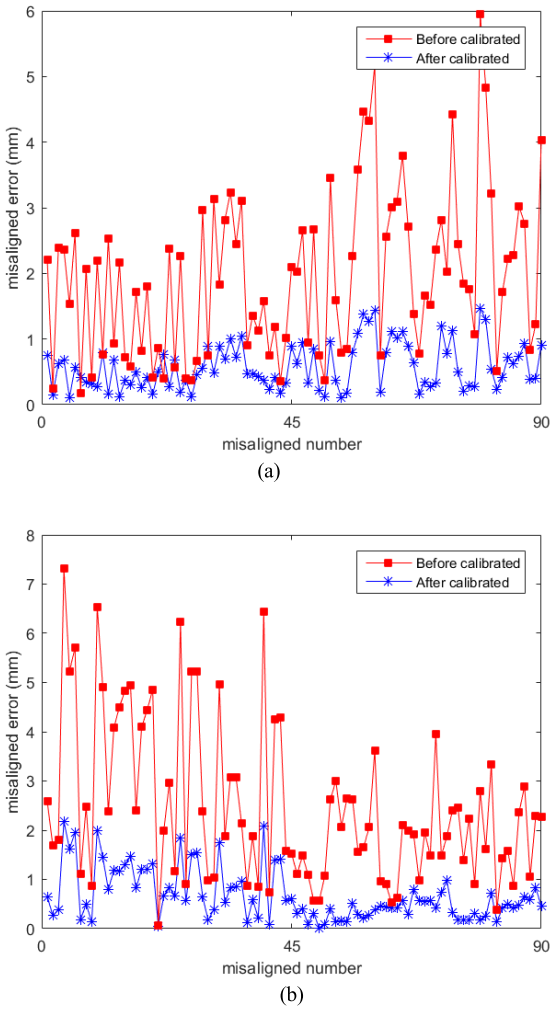

FIGURE 15. The comparative results with two optical axes of: (a) robot 1; (b) robot 2.

D. ROBUSTNESS OF THE PROPOSED METHOD

In order to demonstrate the robustness of the proposed method, two more experiments are built by changing the base-base relative pose ${}^{b_1}\boldsymbol{T}_{b_2}$ and hand-eye relative pose ${}^{c}\boldsymbol{T}_{h}$. The relative poses are approximated to ${}^{b_1}\boldsymbol{T}'_{b_2}$ and ${}^{c}\boldsymbol{T}'_{h}$ respectively in the second experiment, and they are approximated to ${}^{b_1}\boldsymbol{T}''_{b_2}$ and ${}^{c}\boldsymbol{T}''_{h}$ in the third experiment.

$$ {}^{b_1}\boldsymbol{T}'_{b_2} = \begin{bmatrix} -1 & 0 & 0 & 1 \\ 0 & -1 & 0 & 0 \\ 0 & 0 & 1 & 0 \\ 0 & 0 & 0 & 1 \end{bmatrix}, $$

$$ {}^{c}\boldsymbol{T}'_{h} = \begin{bmatrix} 1 & 0 & 0 & -0.6 \\ 0 & 1 & 0 & -0.6 \\ 0 & 0 & 1 & 0.26 \\ 0 & 0 & 0 & 1 \end{bmatrix}, $$

$$
{}^{b_1}\boldsymbol{T}''_{b_2} = \begin{bmatrix} -1 & 0 & 0 & 1.1 \\ 0 & -1 & 0 & 0.2 \\ 0 & 0 & 1 & 0 \\ 0 & 0 & 0 & 1 \end{bmatrix},
$$

$$
{}^{c}\boldsymbol{T}'_{h} = \begin{bmatrix} 1 & 0 & 0 & -0.6 \\ 0 & 1 & 0 & 0.6 \\ 0 & 0 & 1 & 0.26 \\ 0 & 0 & 0 & 1 \end{bmatrix}.
$$

In the second experiment, the left eye of the camera is used. It is important to notice that the distance between the two robot bases should not be too far nor too close, otherwise the constraints $C_i(i = 1, \cdots, 5)$ would not be satisfied. After changing ${}^{b_1}\boldsymbol{T}_{b_2}$ and ${}^{c}\boldsymbol{T}_{h}$, the desired optimal poses of the robots need to be re-generated using the PSO algorithm. In each experiment, two directions of the optical axis and 10 poses aligned to the optical axis in each direction are generated.

In the comparison experiments, only Robot 1 is calibrated. After the feature point are aligned to the optical axis, the joint angles of the passive robots at each alignment position are saved. Using the nominal and calibrated kinematic parameters respectively, the corresponding positions of the passive robot can be calculated based on the forward kinematic model. According to (44), the misaligned error $\boldsymbol{E}$ before and after calibration can be calculated. The comparison results of the misaligned error in the second and third experiments are shown in Fig. 16.

In the second experiment, the average misaligned error reduced from 2.46 mm to 0.70 mm, which decreased 71.37%. In the third experiment, the average misaligned error reduced from 2.42 mm to 0.65 mm, which decreased 73.18%. The results are similar with the validation result in the first experiment. It can be demonstrated that the proposed method is robust to different relative poses.

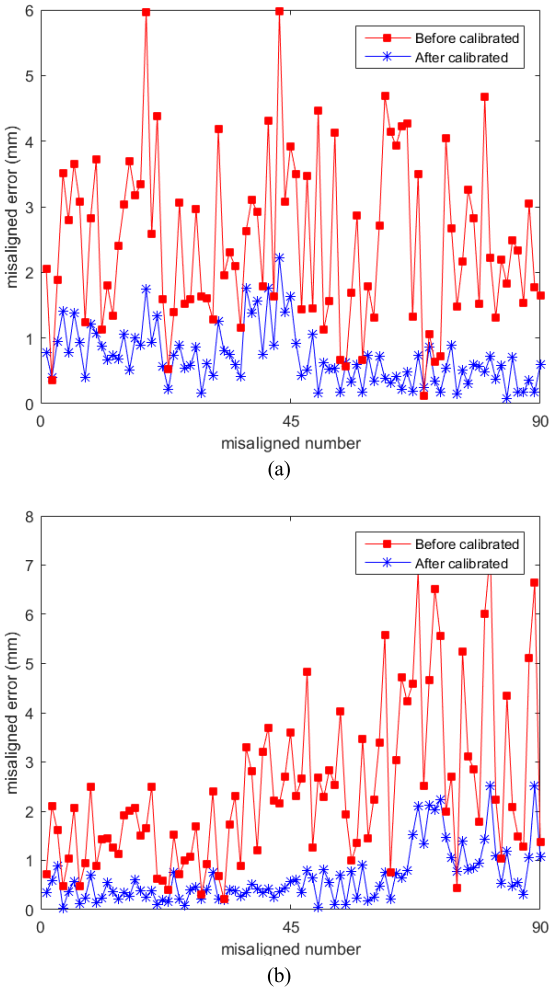

FIGURE 16. The comparison results with two optical axes in the: (a) 2nd experiment; (b) 3rd experiment.

VII. DISCUSSION

The research in [15] and the proposed method in this paper both calibrated the robot kinematic parameters based on virtual straight line constraints. A laser was used in [15] to construct the constraint and an optical sensor is centered on the laser line. Compared with the laser and optical sensor, camera and calibration target used in this paper are easier-to-obtain and used more frequently in the manipulator area. Thanks to plenty researches on machine vision, the vision-based kinematic calibration process is easy to be completed automatically because it is easy to detect the fixed point on the robot EE by the corner detection algorithm [32] and align the fixed point to the optical axis by the visual control method. Moreover, the PSO algorithm is developed to generate the optical poses of the robots under the designed constraints in this paper, which ensures the calibration poses feasible and the measurement errors acceptable.

The calibration method proposed in this paper achieved high positional accuracy of both robots. It is inexpensive and easy to perform. However, this method could be further improved. In the next step, we will put effort into improving the calibration accuracy and reducing the influence of the measurement error. Information fusion techniques, such as Kalman filter and particle filter [33]–[36], are often used to analyze the sensing information and deal with the uncertainty of the sensing systems. The sliding mode estimation method [37] is also a good way to get a good estimation result and improve the robustness of the nonlinear system. These techniques might be good choices for improving the robot calibration method.

VIII. CONCLUSION

A kinematic calibration method for dual-manipulators is proposed in this paper based on virtual line constraint, which is inexpensive, easy to perform and can be accomplished automatically. Firstly, based on the new established kinematic error model, the calibration results are unaffected by the camera's low depth accuracy. Secondly, the PSO algorithm is developed to generate the optimal configurations of both robots, which limits the impact of camera resolution and improves the calibration accuracy. Thirdly, the poses

alignment process is completed automatically based on the visual control method. Then the kinematic parameters are identified by LM algorithm. The effectiveness of the calibration method was verified through experiments on the dual-manipulators system. The average misaligned errors of robot 1 and robot 2 are decreased 85.14% and 89.04% respectively. The comparison experiments demonstrated that the proposed method is robust to different base-base and hand-eye relative pose.

The proposed method can also be used for the single manipulator and multi-manipulators calibration by fixing the camera in the appropriate place. In the future, subsequent works will be continued to simplify the calibration process and shorten the calibration time. We will pay more attention to improving the accuracy and robustness of the developed method by combining the information fusion method. Moreover, the proposed method will be extended to calibrate the whole dual-manipulators system simultaneously, including the kinematics calibration, the base-base calibration and the hand-eye calibration.

REFERENCES

[1] W. Wang, F. Liu, and C. Yun, "Calibration method of robot base frame using unit quaternion form," *Precis. Eng.*, vol. 41, no. 3, pp. 47–54, 2015.

[2] Y. Gan and X. Dai, "Base frame calibration for coordinated industrial robots," *Robot. Auto. Syst.*, vol. 59, nos. 7–8, pp. 563–570, 2011.

[3] M. R. Driels, W. Swayze, and S. Potter, "Full-pose calibration of a robot manipulator using a coordinate-measuring machine," *Int. J. Adv. Manuf. Technol.*, vol. 8, no. 1, pp. 34–41, 1993.

[4] I.-W. Park, B.-J. Lee, S.-H. Cho, Y.-D. Hong, and J.-H. Kim, "Laser-based kinematic calibration of robot manipulator using differential kinematics," *IEEE/ASME Trans. Mechatronics*, vol. 17, no. 6, pp. 1059–1067, Dec. 2012.

[5] A. Nubiola and I. A. Bonev, "Absolute robot calibration with a single telescoping ballbar," *Precis. Eng.*, vol. 38, no. 3, pp. 472–480, 2014.

[6] W. Zhou *et al.*, "Accurate calibration of kinematic parameters in long-reach space manipulator arm," *Manned Spaceflight*, vol. 22, no. 4, pp. 466–470, 2016.

[7] Y. Wang, S. Wang, C. Zhou, and M. Tan, "Kinematics analysis of a 4-DOF underwater manipulator installed on the vehicle," in *Proc. IEEE Int. Conf. Robot. Biomimetics*, Dec. 2016, pp. 993–998.

[8] Y. Meng and H. Zhuang, "Autonomous robot calibration using vision technology," *Robot. Comput. Integr. Manuf.*, vol. 23, no. 4, pp. 436–446, 2007.

[9] G. Du and P. Zhang, "Online robot calibration based on vision measurement," *Robot. Comput. Integr. Manuf.*, vol. 29, no. 6, pp. 484–492, 2013.

[10] X. Zhang, Y. Song, Y. Yang, and H. Pan, "Stereo vision based autonomous robot calibration," *Robot. Auto. Syst.*, vol. 93, pp. 43–51, Jul. 2017.

[11] M. A. Meggiolaro, G. Scriffignano, and S. Dubowsky, "Manipulator calibration using a single endpoint contact constraint," in *Proc. ASME Design Eng. Tech. Conf.*, Baltimore, MD, USA, Sep. 2000, pp. 1–10.

[12] H. Zhuang, S. H. Motaghedi, and Z. S. Roth, "Robot calibration with planar constraints," in *Proc. IEEE Int. Conf. Robot. Autom.*, Detroit, MI, USA, May 1999, pp. 805–810.

[13] A. Joubair and I. A. Bonev, "Kinematic calibration of a six-axis serial robot using distance and sphere constraints," *Int. J. Adv. Manuf. Technol.*, vol. 77, nos. 1–4, pp. 515–523, 2015.

[14] D. J. Bennett and J. M. Hollerbach, "Autonomous calibration of single-loop closed kinematic chains formed by manipulators with passive endpoint constraints," *IEEE Trans. Robot. Autom.*, vol. 7, no. 5, pp. 597–606, Oct. 1991.

[15] W. S. Newman and D. W. Osborn, "A new method for kinematic parameter calibration via laser line tracking," in *Proc. IEEE Int. Conf. Robot. Autom.*, Atlanta, GA, USA, May 1993, pp. 160–165.

[16] C. S. Gatla, R. Lumia, J. Wood, and G. Starr, "An automated method to calibrate industrial robots using a virtual closed kinematic chain," *IEEE Trans. Robot.*, vol. 23, no. 6, pp. 1105–1116, Dec. 2007.

[17] S. Yin, Y. Ren, J. Zhu, S. Yang, and S. Ye, "A vision-based self-calibration method for robotic visual inspection systems," *Sensors*, vol. 13, no. 2, pp. 16565–16582, 2013.

[18] S. Du, J. Ding, and Y. Liu, "Industrial robot kinematic calibration using virtual line-based sphere surface constraint approach," in *Proc. IEEE Int. Conf. Cyber Technol. Automat., Control, Intell. Syst.*, Shenyang, China, Jun. 2015, pp. 48–53.

[19] J. Su, "Base calibration for dual robot system," *Control Theory Appl.*, vol. 15, no. 4, pp. 575–582, 1998.

[20] D. Zhao, Y. Bi, and Y. Ke, "Kinematic modeling and base frame calibration of a dual-machine-based drilling and riveting system for aircraft panel assembly," *Int. J. Adv. Manuf. Technol.*, vol. 94, nos. 5–8, pp. 1873–1884, 2017.

[21] L. Wu, J. Wang, L. Qi, K. Wu, H. Ren, and M. Q.-H. Meng, "Simultaneous hand–eye, tool–flange, and robot–robot calibration for comanipulation by solving the $AXB = YCZ$ problem," *IEEE Trans. Robot.*, vol. 32, no. 2, pp. 413–428, Apr. 2016.

[22] R. G. Bonitz and T. C. Hsia, "Calibrating a multi-manipulator robotic system," *IEEE Robot. Autom. Mag.*, vol. 4, no. 1, pp. 18–22, Mar. 1997.

[23] Y. Qiao *et al.*, "A novel calibration method for multi-robots system utilizing calibration model without nominal kinematic parameters," *Precis. Eng.*, vol. 50, pp. 211–221, Oct. 2017.

[24] D. Zhao, Y. Bi, and Y. Ke, "A united kinematic calibration method for a dual-machine system," *Assem. Autom.*, vol. 38, no. 2, pp. 226–238, 2018.

[25] Z. Zhang, "A flexible new technique for camera calibration," *IEEE Trans. Pattern Anal. Mach. Intell.*, vol. 22, no. 11, pp. 1330–1334, Mar. 2000.

[26] K. Schröer, S. L. Albright, and M. Grethlein, "Complete, minimal and model-continuous kinematic models for robot calibration," *Robot. Comput.-Integr. Manuf.*, vol. 13, no. 1, pp. 73–85, 1997.

[27] H. Zhuang, Z. S. Roth, and F. Hamano, "A complete and parametrically continuous kinematic model for robot manipulators," *IEEE Trans. Robot. Autom.*, vol. 8, no. 4, pp. 451–463, Aug. 1992.

[28] H. Zhuang, L. K. Wang, and Z. S. Roth, "Error-model-based robot calibration using a modified CPC model," *Robot. Comput.-Integr. Manuf.*, vol. 10, no. 4, pp. 287–299, 1993.

[29] R. He, Y. Zhao, S. Yang, and S. Yang, "Kinematic-parameter identification for serial-robot calibration based on POE formula," *IEEE Trans. Robot.*, vol. 26, no. 3, pp. 411–423, Jun. 2010.

[30] S. A. Hayati, "Robot arm geometric link parameter estimation," in *Proc. 22nd IEEE Conf. Decis. Control*, Dec. 1983, pp. 1477–1483.

[31] A. Joubair and I. A. Bonev, "Comparison of the efficiency of five observability indices for robot calibration," *Mech. Mach. Theory*, vol. 70, no. 6, pp. 254–265, 2013.

[32] E. Rosten, R. Porter, and T. Drummond, "Faster and better: A machine learning approach to corner detection," *IEEE Trans. Pattern Anal. Mach. Intell.*, vol. 32, no. 1, pp. 105–119, Jan. 2010.

[33] G. Du and P. Zhang, "Online serial manipulator calibration based on multisensory process via extended Kalman and particle filters," *IEEE Trans. Ind. Electron.*, vol. 61, no. 12, pp. 6852–6859, Dec. 2014.

[34] G. Du, P. Zhang, and D. Li, "Human–manipulator interface based on multisensory process via Kalman filters," *IEEE Trans. Ind. Electron.*, vol. 61, no. 10, pp. 5411–5418, Oct. 2014.

[35] G. Du, P. Zhang, and X. Liu, "Markerless human-manipulator interface using leap motion with interval Kalman filter and improved particle filter," *IEEE Trans. Ind. Informat.*, vol. 12, no. 2, pp. 694–704, Apr. 2016.

[36] G. Du and P. Zhang, "A markerless human-robot interface using particle filter and Kalman filter for dual robots," *IEEE Trans. Ind. Electron.*, vol. 62, no. 4, pp. 2257–2264, Apr. 2015.

[37] H. Alwi, C. Edwards, and C. P. Tan, "Sliding mode estimation schemes for incipient sensor faults," *Automatica*, vol. 45, no. 7, pp. 1679–1685, 2009.

QIDAN ZHU received the B.S. degree in automatic control and the M.S. and Ph.D. degrees in control theory and control engineering from Harbin Engineering University, Harbin, China, in 1985, 1987, and 2001, respectively, where he is currently a Professor with the College of Automation.

His research interests include robotics, computer vision, control theory, and engineering.

XINRU XIE received the B.S. degree in automation and the M.S. degree in control science and engineering from Harbin Engineering University, Harbin, China, in 2014 and 2016, respectively, where she is currently pursuing the Ph.D. degree in control science and engineering.

Her main research interests include robotics and computer vision.

CHAO LI received the B.S. degree in automation and the M.S. degree in control science and engineering from Harbin Engineering University, Harbin, China, in 2013 and 2015, respectively, where he is currently pursuing the Ph.D. degree in control science and engineering.

His main research interests include the compliant control of the robot and deep learning.

GUIHUA XIA received the B.S. degree in automatic control and the M.S. and Ph.D. degrees in management science and engineering from Harbin Engineering University, Harbin, China, in 1983, 2000, and 2006, respectively, where he is currently a Professor with the College of Automation.

His research interests include robotics and intelligent ship.

QI LIU received the B.S. degree in mechanical and electrical engineering from Harbin Engineering University, Harbin, China, in 2015. He is currently an Engineer with the Institute of Chemical Materials, China Academy of Engineering Physics, China.

His research interests include bionic robots.